Optical-resolution photoacoustic microscopy of oxygen saturation with nonlinear compensation

CHAO LIU,[1,2] YIZHI LIANG,[3,4] AND LIDAI WANG[1,2,5]

[1]*Department of Biomedical Engineering, City University of Hong Kong, 83 Tat Chee Ave, Kowloon, Hong Kong SAR, China*
[2]*City University of Hong Kong Shenzhen Research Institute, Yuexing Yi Dao, Nanshan District, China*
[3]*Guangdong Provincial Key Laboratory of Optical Fiber Sensing and Communications, Institute of Photonics Technology, Jinan University, Guangzhou 510632, China*
[4]*liangyizhi88528@gmail.com*
[5]*lidawang@cityu.edu.hk*

Abstract: Optical-resolution photoacoustic microscopy (OR-PAM) of oxygen saturation (sO_2) offers high-resolution functional information on living tissue. Limited by the availability of high-speed multi-wavelength lasers, most OR-PAM systems use wavelengths around 532nm. Blood has high absorption coefficients in this spectrum, which may cause absorption saturation and induce systematic errors in sO_2 imaging. Here, we present nonlinear OR-PAM that compensates for the absorption saturation in sO_2 imaging. We model the absorption saturation at different absorption coefficients and ultrasonic bandwidths. To compensate for the absorption saturation, we develop an OR-PAM system with three optical wavelengths and implement a nonlinear algorithm to compute sO_2. Phantom experiments on bovine blood validate that the nonlinear OR-PAM can improve the sO_2 accuracy by up to 0.13 for fully oxygenated blood. *In vivo* sO_2 imaging has been conducted in the mouse ear. The nonlinear sO_2 results agree with the normal physiological values. These results show that the absorption saturation effect can be compensated for in nonlinear OR-PAM, which improves the accuracy of functional photoacoustic imaging.

1. Introduction

Optical-resolution photoacoustic microscopy (OR-PAM) converts absorbed optical energy into ultrasonic wave, offering optical absorption contrast at sub-cellular spatial resolutions [1–5]. Taking advantages of noninvasive and label-free imaging, OR-PAM has been widely applied to map functional parameters, e.g., blood flow, oxygen saturation (sO_2), and metabolic rate of oxygen, in living tissue [6–13]. When a laser impulse illuminates the blood vessel, the dominant absorbing molecules, deoxygenated hemoglobin (HbR) and oxygenated hemoglobin (HbO$_2$) generate photoacoustic (PA) signal, whose amplitude is a function of the molar extinction coefficients and the molecular concentrations [14–23]. PA measurements at two or more wavelengths allow the computation of the sO_2 [22–28].

Conventional sO_2 imaging assumes that the PA amplitude is a linear function of the absorption coefficient. However, when the absorption coefficient is high, the PA amplitude may become a nonlinear function of the absorption coefficient, referred to as the absorption saturation effect [29]. In such a case, the linear PA assumption will not be accurate and may lead to biased sO_2 measurements. The absorption saturation is related to the absorber's thickness, the axial resolution, and the optical wavelength [30]. In *in vivo* imaging, the absorber's thickness varies among different blood vessels. The axial resolution and the optical wavelengths usually compromise with other parameters, such as imaging depth, sensitivity, laser energy, and laser pulse repetition rate. For instance, to increase the imaging depth and detection sensitivity, OR-PAM usually uses a broadband ultrasound transducer with a central

frequency of 50 MHz or lower, which limits the axial resolution to tens of microns. In high-speed OR-PAM, commercial high pulse-repetition-rate lasers with high pulse energy usually have a limited choice of wavelengths around 532nm [31, 32]. The absorption coefficient of 100% oxygenated blood at 532nm is ~237 cm^{-1}, which may cause absorption saturation in photoacoustic imaging. Therefore, compensation for the absorption saturation may improve the accuracy in OR-PAM sO_2 imaging.

Here, we develop a nonlinear OR-PAM technique to compensate for the absorption saturation in sO_2 imaging. We use a nonlinear model to compute the sO_2 from the PA measurements. We compare the nonlinear method with the linear one in numerical simulation. When absorption saturation exists, the nonlinear model can determine the sO_2 more accurately than the linear model. Solving the nonlinear model requires photoacoustic measurements at three or more optical wavelengths. We develop a three-wavelength pulsed laser to measure the sO_2. The laser has a 1-MHz pulse repetition rate at each wavelength, 150-ns wavelength-switching time, and 60-nJ or higher pulse energy at each wavelength. Phantom experiments on bovine blood and *in vivo* experiments in the mouse ear demonstrate the improved accuracy of nonlinear sO_2 imaging.

2. Methods

2.1 Absorption saturation

Under thermal and stress confinement, the PA amplitude from a voxel can be written as

$$PA = k\Gamma\eta F[1-\exp(-\mu_a \Delta z)], \tag{1}$$

where k is a constant factor related to the PA detection sensitivity, Γ is the local Grueneisen parameter, η is the percentage of absorbed energy that converts into heat, F is the fluence at the top surface of the voxel, μ_a is the absorption coefficient and is assumed as uniform in the voxel, and Δz is the voxel size in the axial direction.

If the absorption coefficient is low, and the axial resolution is high, i.e. $\mu_a \Delta z$ is close to zero, the PA amplitude can be approximated as

$$PA = k\Gamma\eta F\mu_a \Delta z, \tag{2}$$

In this case, the PA amplitude is a linear function of the absorption coefficient μ_a. In the blood, μ_a is a linear function of the concentrations of HbO$_2$ and HbR. Thus, we can measure PA signals at two or more optical wavelengths and compute the sO_2 based on the approximated linear model in Eq. (2).

However, if the absorption is strong, or the axial resolution is low, i.e. $\mu_a \Delta z$ is not close to zero, the PA amplitude remains a nonlinear function of the absorption coefficient, which is referred to as absorption saturation. Most fast OR-PAM systems use wavelengths around 532nm, leading to strong absorption in the blood. In addition, the axial resolution is limited to tens of microns. In such a case, the use of linear PA model will cause a systematic error in the sO_2 calculation. In contrast, the nonlinear Eq. (1) shows an accurate relationship between the PA signal and the absorption coefficient even when the absorption saturation exists.

2.2 Nonlinear method for sO_2 measurement

To compensate for the saturation effect, the nonlinear model in Eq. (1) is used to measure the sO_2. The absorption coefficient of blood at one wavelength can be written as $\mu_a = rC_{HbT}[sO_2\varepsilon^{oxy} + (1-sO_2)\varepsilon^{de}]$, where r is a known constant coefficient [34], and C_{HbT} is the total hemoglobin concentration, and ε^{oxy} and ε^{de} are the molar extinction coefficients of HbO$_2$ and HbR at the excitation wavelength. Substituting μ_a into Eq. (1), we can write the PA amplitude as a nonlinear function of sO_2 as

$$PA = k\Gamma\eta F[1 - \exp(-r(sO_2\varepsilon^{oxy} + (1-sO_2)\varepsilon^{de})C_{HbT}\Delta z)]. \tag{3}$$

In superficial tissue, we assume that the local fluence F can be estimated from the fluence on the tissue surface. In the following text, the fluence is set to the unit and is not explicitly expressed in the equations. Equation (3) has three unknowns, sO_2, $rC_{HbT}\Delta z$, and $k\Gamma\eta$. To solve them, we measure the PA signals at three wavelengths, λ_1, λ_2, and λ_3, obtaining PA_1, PA_2, and PA_3.

An iterative algorithm is developed to solve the sO_2. Each iteration takes two steps. In the first step of the ith iteration, we compute the ratio of PA_{1_i} to PA_{2_i} as

$$\frac{PA_{1-i}}{PA_{2-i}} = \frac{1 - \exp[-u_i(sO_{2\_i}\varepsilon_1^{oxy} + (1-sO_{2\_i})\varepsilon_1^{de})]}{1 - \exp[-u_i(sO_{2\_i}\varepsilon_2^{oxy} + (1-sO_{2\_i})\varepsilon_2^{de})]}, \tag{4}$$

where $u_i = rC_{HbT_i}\Delta z_i$. Substituting the sO_2 value from the previous iteration, i.e., sO_{2_i-1}, into Eq. (4), we can solve the unknown u_i. In the second step, we compute the ratio of PA_{3_i} to PA_{2_i} as

$$\frac{PA_{3-i}}{PA_{2-i}} = \frac{1 - \exp[-u_i(sO_{2\_i}\varepsilon_3^{oxy} + (1-sO_{2\_i})\varepsilon_3^{de})]}{1 - \exp[-u_i(sO_{2\_i}\varepsilon_2^{oxy} + (1-sO_{2\_i})\varepsilon_2^{de})]}, \tag{5}$$

Substituting u_i into Eq. (5), we can solve an updated sO_{2_i}.

The initial sO_{2_0} is estimated from the linear model in Eq. (2). After several iterations, the sO_2 value converges to a stable value. When the $|sO_{2\_i} - sO_{2\_i-1}|$ is smaller than a threshold value (0.001 in this work), we terminate the iteration.

2.3 OR-PAM system

The nonlinear method requires PA measurements at three or more wavelengths. Here we develop an OR-PAM system with a 1-MHz three-wavelength pulsed laser. A schematic diagram of the OR-PAM system is illustrated in Fig. 1. A nanosecond pulsed laser (wavelength 532 nm, VPFL-G-20, Spectra-Physics) is used as a pump laser to generate another two wavelengths via stimulated Raman scattering (SRS). The highest pulse repetition rate of the pump laser is 1 MHz. The pulse width is set at 7 ns. The maximum pulse energy is 100 μJ, which is sufficient for inducing SRS in a single-mode fiber. The 532-nm pump beam is split into a direct path and a Raman path using a halfwave plate (HWP1) and a polarizing beamsplitter. The direct path is coupled into an OR-PAM probe without significant time delay. In the Raman path, the pump beam is coupled into a 30-meter polarization-maintaining single-mode fiber (SM fiber1, 30m, PM-S405-XP, NUFERN) through a fiber coupler (MBT621D, Thorlabs Inc). The coupling efficiency is ~55%. The 30-meter fiber will delay this path by 150 ns. A halfwave plate (HWP2) is placed before the fiber coupler to adjust the incident polarization state so that the SRS efficiency in the fiber is maximized. Via adjusting the incident power, the 30-meter fiber can generate 545 nm and 558 nm wavelengths via SRS effect. A dichroic mirror (DM1, 69-203, Edmund Optics Inc) is placed after the SRS fiber output to reflect the 558-nm light but transmit the 532-nm and 545-nm light. The 558-nm pulse further passes a halfwave plate (HWP3) and is coupled into another 30-meter polarization-maintaining single-mode fiber (SM fiber2, 30m, HB450-SC, FIBERCORE) for time delay. The halfwave plate adjusts the polarization state to suppress the SRS effect in the delay fiber. After the 30-meter delay, the 558-nm beam is combined with the 545-nm beam using another dichroic mirror (DM2, 69-203, Edmund Optics Inc). A long-pass filter (LPF, T540lpxr, CHROMA) is placed before dichroic mirror 2 to reject the remaining 532-nm light in the delay path. At the last stage, a 90/10 beam splitter combines the direct 532-nm beam with the delayed 545/558-nm beam. The three beams are coupled into the OR-PAM probe via a 2-meter single-mode fiber.
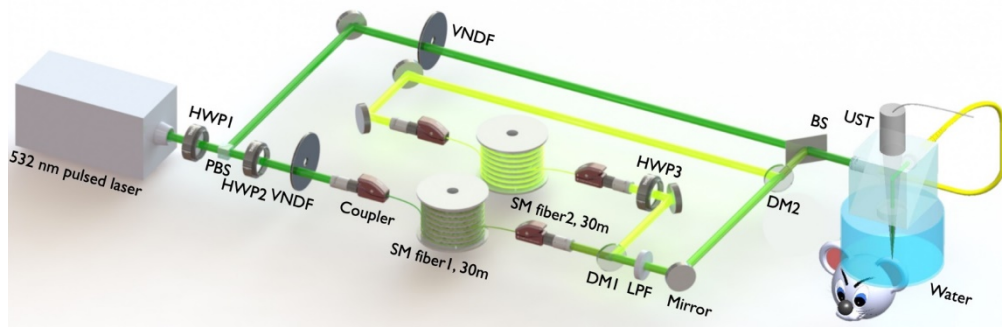
Fig. 1. Schematic diagram of OR-PAM system with a three-wavelength pulsed laser. BS: beam splitter R/T: 90/10, DM1&DM2: dichroic mirror 550 nm short-pass, HWP1-3: half-wave plate, LPF: 540 nm long-pass filter, PBS: polarization beam splitter, SM fiber 1-2: single-mode fiber, UST: ultrasonic transducer, VNDF: variable neutral density filter.

In the OR-PAM probe, the pulsed laser beam is focused into the sample to induce photoacoustic waves. A 50-MHz ultrasound transducer (V214-BC-RM, Olympus-NDT) focuses on the sample and is confocally aligned with the optical focus to optimize the detection sensitivity. A low pass filter (SLP-50 + , Mini Circuits) is used to filter PA signal. The bandwidth of the filtered PA signal determines the axial resolution as 50 μm. Raster scanning the photoacoustic probe generates volumetric images. Detailed information of the OR-PAM probe can be referred to in the previous papers [16,27,35].

The pulse energy of each wavelength is about 60 nJ at the sample surface, which is comparable to the pulse energies used in other reported OR-PAM systems [16,27,35]. The time delays of the 532nm, 545nm, and 558nm pulses are 0, 150ns, and 300ns respectively, enabling temporal separation of the three PA signals. Figure 2 (a) shows laser spectrum measured with an optical spectrometer (USB 2000 + , Ocean Optics). The linewidths of the 532, 545, and 558 nm wavelengths are 1.6, 2.4, and 4.4nm, respectively. Normalized molar extinction coefficients of HbO_2 and HbR are plotted in Fig. 2(a). The 532-nm wavelength is close to an isosbestic point, the 545-nm wavelength is an isosbestic point, and the 558-nm wavelength is more absorptive for HbR than HbO_2. The different absorption coefficients at the three wavelengths make it possible to implement the nonlinear sO_2 model.

3. Results and discussion

3.1 Numerical simulation

We numerically evaluate the impact of absorption saturation on the accuracy of sO_2 measurement under different sO_2 values and different axial resolutions shown. The axial resolutions are set at 10 μm, 30 μm, 60 μm, and 120μm. Figure 2(b) shows that a lower axial resolution or a larger absorption coefficient may lead to stronger absorption saturation and nonlinearity. The total hemoglobin concentration is set at 160 g/liter. Using these parameters, we generate PA amplitudes at 3 wavelengths, 532 nm, 545 nm, and 558 nm by Eq. (1). The generated PA amplitudes at the three wavelengths are used to compute the sO_2 with the nonlinear method. The 532-nm and 558-nm PA amplitudes are used in the linear sO_2 computation. The nonlinear iterations converge after the second iteration. Because we use the same nonlinear model to generate simulation data and compute sO_2, in this simulation, all sO_2 results computed with the nonlinear method are the same as the set sO_2 values.

The linear sO_2 values are compared with the set sO_2, as shown in Fig. 2(c). When the set sO_2 value is greater than 0.57, the linear method underestimates the sO_2 value. When the sO_2 is smaller than 0.57, the linear method overestimates the sO_2 value. At $sO_2 = 0.57$, because the absorption coefficients at 532nm and 558nm are the same, the calculated sO_2 by linear method equals to the set value. In such a case, the saturation effect causes the same fractional

PA changes at the two wavelengths and induces no errors to the linear sO_2 results. In other sO_2 values, the linear method leads to biased results due to absorption saturation. In contrast, the nonlinear method can compensate for absorption saturation.

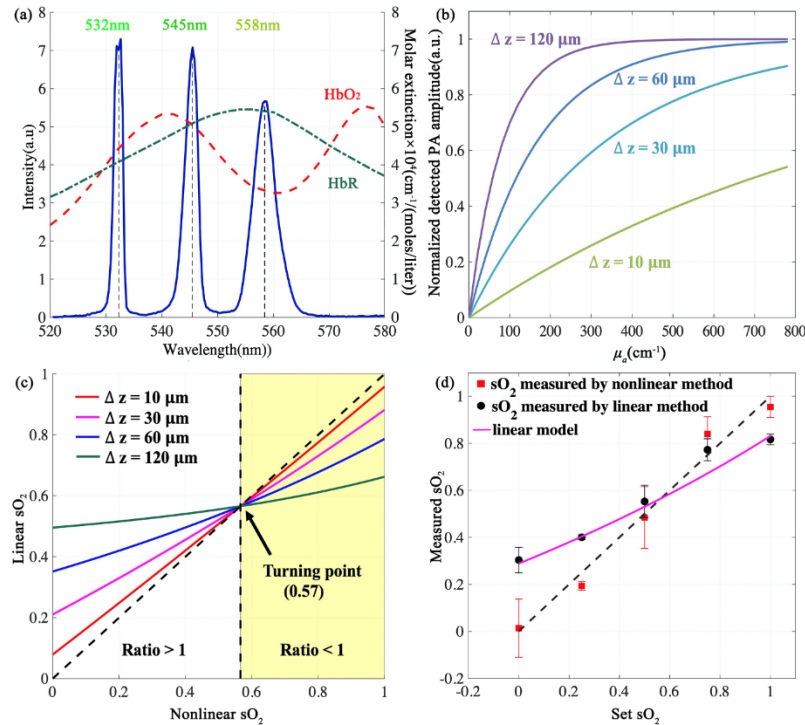## 3.2 In vitro validation of nonlinear method

Fig. 2. (a) Spectrum of the three-wavelength stimulated-Raman-scattering laser. (b) Absorption saturation effect with different axial resolutions and absorption coefficients. (c) Impact of absorption saturation effect on sO_2 accuracy using linear method. The nonlinear sO_2 results is the same as the set values. The tilted dashed line represents an ideal case that the linear sO_2 results are unbiased. (d) In vitro sO_2 measurement of bovine blood samples using both linear and nonlinear models. Sample size = 5.

We validate the nonlinear method on blood phantoms. Sealed anticoagulant bovine blood fills 5 transparent plastic bags. Each bag contains 10-ml blood. The sO_2 values of the blood samples are set via adding different dosages of sodium dithionite [36,37]. The minimum concentration of sodium dithionite to change sO_2 from 1 to 0 is 2.5 mg/ml. Via changing the chemical concentration, sO_2 of the samples are set to 0, 0.25, 0.5, 0.75, and 1. Nitrogen gas is used to remove air in the bag.

   Figure 2(d) shows the sO_2 results of the in vitro experiments. Both linear and nonlinear methods are used to compute sO_2. Each sO_2 result was first averaged 100 times in one bag and then was averaged over 5 samples. For fully oxygenated blood samples, the linear method gives an averaged sO_2 value of 0.82 ± 0.02 (SD), and the nonlinear result is 0.95 ± 0.04(SD), showing an accuracy improvement of 0.13. For the set sO_2 of 0.75, 0.5, 0.25, 0, the nonlinear method can improve the linear results by 0.07, 0.08, 0.21, 0.28, respectively. The phantom results validate that the nonlinear method can compensate for the absorption saturation effect in the sO_2 measurement.

3.3 In vivo sO_2 imaging

We compare the linear and nonlinear sO_2 imaging in the mouse ear. The protocol of animal experiments has been approved by the animal ethical committee of the City University of Hong Kong. PA images are acquired at three wavelengths, 532nm, 545nm, and 558nm. For each wavelength, the pulse energy is 60 nJ, the laser repetition rate is 4 kHz, and 4000×3500 A-lines are acquired for a 3D *in vivo* image. The step size in the lateral direction is 2.5 μm. The field of view of the acquired image is 10×8.75 mm^2 in the lateral plane. The time to acquire a 3D image is 3500 seconds. Figure 3(a) and (b) show a maximum-amplitude-projected image and a close-up image of the microvasculature acquired at 532nm. The capillaries can be resolved with a signal-to-noise ratio of 10.6 dB. The sO_2 values are calculated with the linear and nonlinear methods, as shown in Fig. 3(d) and (e). A 5×5-pixel moving-average filter is used to smooth the sO_2 images. In both the linear and nonlinear sO_2 images, the arteries and veins can be differentiated. In the arteries, the linear method gives results obvious lower than the nonlinear ones. To compare the linear and nonlinear results, we select the sO_2 values in three artery-vein pairs as labeled in the dashed boxes in Fig. 3(d) and (e). Figure 3(c) shows the averaged sO_2 values of each artery and vein. The sO_2 values by linear method are consistently smaller than the ones by nonlinear method. In Fig. 3(c), we only quantify trunk vessels. sO_2 values in those vessels are greater than 0.57. According to numerical simulation, when sO_2 is greater than 0.57, linear method underestimates sO_2. Thus, both the trunk arteries and veins show higher sO_2 in the nonlinear result than those in the linear one. We do find some small vessels have lower sO_2 (<0.57). However, if the vessel diameter is smaller than the axial resolution, the absorption saturation effect becomes not obvious. In those vessels, we do not observe significant difference between the nonlinear and the linear results.
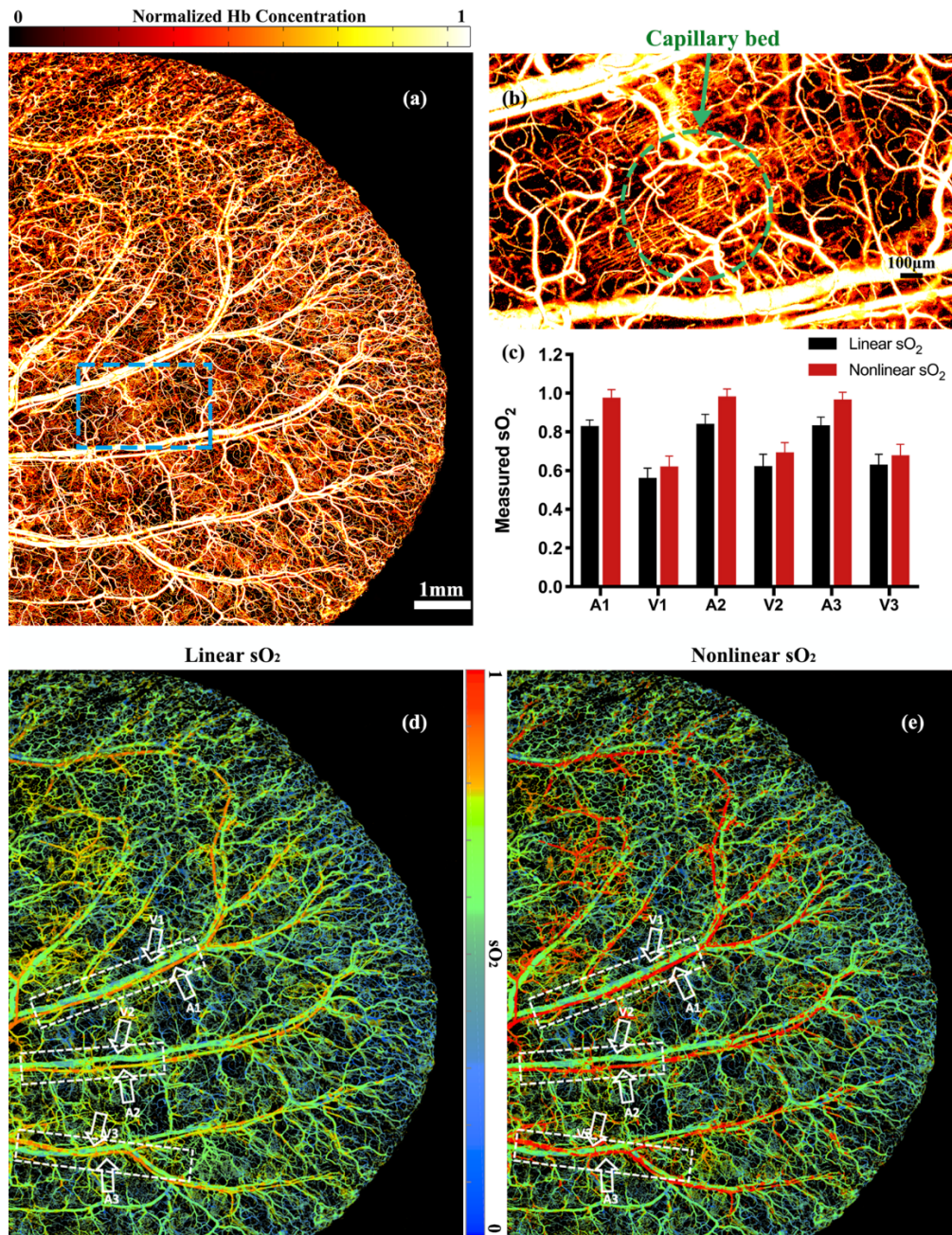
Fig. 3. (a) *In vivo* imaging of the total hemoglobin concentration in the mouse ear. (b) Close-up of the blue dashed box in (a). (c) Comparison of the linear and nonlinear sO_2 values in three artery-vein pairs as labeled in the white dashed boxes in (d) and (e). Error bars are standard derivations. (d) Linear sO_2 image of the mouse ear. (e) Nonlinear sO_2 image of the mouse ear.

The OR-PAM system has an axial resolution of 50 μm. In the simulation results in Fig. 2(c), at an axial resolution of 50 μm, the set sO_2 value is about 1.19 times of the one by linear method when the sO_2 is 1, and is 1.07 times of the one by linear method when the sO_2 value is 0.66. The *in vivo* results in Fig. 3(c) show a similar trend with the simulation results.

The *in vivo* experiments demonstrate that the nonlinear method can compensate for the absorption saturation.

4. Conclusion

We develop a nonlinear method to compensate for the absorption saturation in OR-PAM sO_2 imaging. The absorption saturation effect is modeled and simulated with different sO_2 values and axial resolutions. Simulation results show that the linear sO_2 method may lead to systemic errors when the absorption saturation exists. In comparison, the nonlinear method can compensate for this error. Absorption saturation has been used to measure sO_2 based on saturation intensity or acoustic spectral analysis [38,39]. However, they may either require a high optical pulse energy or are not applicable to small blood vessels due to complicated acoustic spectrum. Our method is not limited by either the pulse energy or the vessel size. Conclusively, we develop an OR-PAM system with a three-wavelength pulsed laser to implement the nonlinear sO_2 imaging. Phantom experiments on bovine blood samples validate that the nonlinear method can improve sO_2 accuracy. We demonstrate nonlinear sO_2 imaging in the mouse ear. In normal physiological conditions, a literature reports the sO_2 values in the arteries are about 0.95~0.99 and the sO_2 values in the peripheral vein are about 0.70~0.80 [40]. The nonlinear sO_2 results are closer to these values than the linear results. The nonlinear sO_2 imaging method can reduce the systemic error caused by absorption saturation. We expect this technical advance in functional imaging may further expand the biomedical application of OR-PAM.

Funding

Disclosures

The authors declare that there are no conflicts of interest related to this article.

References

1. L. V Wang, H.-I. Wu, and B. R Masters, *Biomedical Optics: Principles and Imaging* (Wiley, 2008), p. 13.
2. S. Hu, "Optical-resolution photoacoustic microscopy: auscultation of biological systems at the cellular level," Biophys. J. **105**, 841 (2010).
3. L. V. Wang and J. Yao, "A practical guide to photoacoustic tomography in the life sciences," Nat. Methods **13**(8), 627–638 (2016).
4. J. Yao and L. V. Wang, "Photoacoustic microscopy," Laser Photonics Rev. **7**(5), 758–778 (2013).
5. C. Kim, C. Favazza, and L. V. Wang, "In Vivo Photoacoustic Tomography of Chemicals: High-Resolution Functional and Molecular Optical Imaging at New Depths," Chem. Rev. **110**(5), 2756–2782 (2010).
6. J. Yao, K. I. Maslov, Y. Zhang, Y. Xia, and L. V. Wang, "Label-free oxygen-metabolic photoacoustic microscopy in vivo," J. Biomed. Opt. **16**(7), 076003 (2011).
7. C. Yeh, S. Hu, J. Liang, L. Li, B. Soetikno, Z. H. Lu, R. E. Sohn, K. Maslov, J. M. Arbeit, and L. V Wang, "Optical-resolution photoacoustic microscopy of the metabolic rate of oxygen in a mouse renal tumor model," in *Photons Plus Ultrasound: Imaging and Sensing 2015* (International Society for Optics and Photonics, 2015), 9323, p. 93233H.
8. J. Laufer, D. Delpy, C. Elwell, and P. Beard, "Quantitative spatially resolved measurement of tissue chromophore concentrations using photoacoustic spectroscopy: application to the measurement of blood oxygenation and haemoglobin concentration," Phys. Med. Biol. **52**(1), 141–168 (2007).
9. M. Moothanchery, A. Sharma, and M. Pramanik, "Switchable Acoustic and Optical Resolution Photoacoustic Microscopy for In Vivo Small-animal Blood Vasculature Imaging," J. Vis. Exp. **124**, e55810 (2017).
10. Y. Jiang, A. Forbrich, T. Harrison, and R. J. Zemp, "Blood oxygen flux estimation with a combined photoacoustic and high-frequency ultrasound microscopy system: a phantom study," J. Biomed. Opt. **17**(3), 036012 (2012).
11. C. Yin, G. Wen, C. Liu, B. Yang, S. Lin, J. Huang, P. Zhao, S. H. D. Wong, K. Zhang, X. Chen, G. Li, X. Jiang, J. Huang, K. Pu, L. Wang, and L. Bian, "Organic Semiconducting Polymer Nanoparticles for Photoacoustic Labelling and Tracking of Stem Cells in the Second Near-Infrared Window," ACS Nano **2018**, 12201 (2018).

12. J. Rebling, H. Estrada, S. Gottschalk, G. Sela, M. Zwack, G. Wissmeyer, V. Ntziachristos, and D. Razansky, "Dual-wavelength hybrid optoacoustic-ultrasound biomicroscopy for functional imaging of large-scale cerebral vascular networks," J. Biophotonics **11**(9), e201800057 (2018).

13. T. J. Allen, O. Ogunlade, E. Zhang, and P. C. Beard, "Large area laser scanning optical resolution photoacoustic microscopy using a fibre optic sensor," Biomed. Opt. Express **9**(2), 650–660 (2018).

14. K. Maslov, H. F. Zhang, and L. V. Wang, "Effects of wavelength-dependent fluence attenuation on the noninvasive photoacoustic imaging of hemoglobin oxygen saturation in subcutaneous vasculaturein vivo," Inverse Probl. **23**(6), S113–S122 (2007).

15. R. Hochuli, P. C. Beard, and B. Cox, "Effect of wavelength selection on the accuracy of blood oxygen saturation estimates obtained from photoacoustic images," Proc. SPIE **9323**, 93231V (2015).

16. L. Wang, K. Maslov, and L. V. Wang, "Single-cell label-free photoacoustic flowoxigraphy in vivo," Proc. Natl. Acad. Sci. U.S.A. **110**(15), 5759–5764 (2013).

17. A. Hussain, W. Petersen, J. Staley, E. Hondebrink, and W. Steenbergen, "Quantitative blood oxygen saturation imaging using combined photoacoustics and acousto-optics," Opt. Lett. **41**(8), 1720–1723 (2016).

18. H. F. Zhang, K. Maslov, M. Sivaramakrishnan, G. Stoica, and L. V. Wang, "Imaging of hemoglobin oxygen saturation variations in single vessels in vivo using photoacoustic microscopy," Appl. Phys. Lett. **90**(5), 053901 (2007).

19. T. Wang, N. Sun, R. Cao, B. Ning, R. Chen, Q. Zhou, and S. Hu, "Multiparametric photoacoustic microscopy of the mouse brain with 300-kHz A-line rate," Neurophotonics **3**(4), 045006 (2016).

20. P. K. Upputuri, K. Sivasubramanian, C. S. K. Mark, and M. Pramanik, "Recent developments in vascular imaging techniques in tissue engineering and regenerative medicine," BioMed Res. Int. **2015**, 783983 (2015).

21. P. H. Reza, K. Bell, W. Shi, J. Shapiro, and R. J. Zemp, "Deep non-contact photoacoustic initial pressure imaging," Optica **5**(7), 814 (2018).

22. C. Lee, M. Jeon, M. Y. Jeon, J. Kim, and C. Kim, "In vitro photoacoustic measurement of hemoglobin oxygen saturation using a single pulsed broadband supercontinuum laser source," Appl. Opt. **53**(18), 3884–3889 (2014).

23. S. Huang, P. K. Upputuri, H. Liu, M. Pramanik, and M. Wang, "A dual-functional benzobisthiadiazole derivative as an effective theranostic agent for near-infrared photoacoustic imaging and photothermal therapy," J. Mater. Chem. B Mater. Biol. Med. **4**(9), 1696–1703 (2016).

24. S. Gottschalk, T. F. Fehm, X. L. Deán-Ben, V. Tsytsarev, and D. Razansky, "Correlation between volumetric oxygenation responses and electrophysiology identifies deep thalamocortical activity during epileptic seizures," Neurophotonics **4**(1), 011007 (2016).

25. P. Hajireza, A. Forbrich, and R. Zemp, "In-Vivo functional optical-resolution photoacoustic microscopy with stimulated Raman scattering fiber-laser source," Biomed. Opt. Express **5**(2), 539–546 (2014).

26. G. Diot, A. Dima, and V. Ntziachristos, "Multispectral opto-acoustic tomography of exercised muscle oxygenation," Opt. Lett. **40**(7), 1496–1499 (2015).

27. Y. Liang, L. Jin, B.-O. Guan, and L. Wang, "2 MHz multi-wavelength pulsed laser for functional photoacoustic microscopy," Opt. Lett. **42**(7), 1452–1455 (2017).

28. R. J. Paproski, A. Heinmiller, K. Wachowicz, and R. J. Zemp, "Multi-wavelength photoacoustic imaging of inducible tyrosinase reporter gene expression in xenograft tumors," Sci. Rep. **4**(1), 5329 (2015).

29. J. Wang, T. Liu, S. Jiao, R. Chen, Q. Zhou, K. K. Shung, L. V. Wang, and H. F. Zhang, "Saturation effect in functional photoacoustic imaging," J. Biomed. Opt. **15**(2), 021317 (2010).

30. H. F. Zhang, K. Maslov, and L. V. Wang, "In vivo imaging of subcutaneous structures using functional photoacoustic microscopy," Nat. Protoc. **2**(4), 797–804 (2007).

31. P. Hajireza, A. Forbrich, and R. J. Zemp, "Multifocus optical-resolution photoacoustic microscopy using stimulated Raman scattering and chromatic aberration," Opt. Lett. **38**(15), 2711–2713 (2013).

32. L. Xu, S. Alam, Q. Kang, D. P. Shepherd, and D. J. Richardson, "Raman-shifted wavelength-selectable pulsed fiber laser with high repetition rate and high pulse energy in the visible," Opt. Express **25**(1), 351–356 (2017).

33. R. J. Hill and W. Konigsberg, "The structure of human hemoglobin. IV. The chymotryptic digestion of the alpha chain of human hemoglobin," J. Biol. Chem. **237**(10), 3151–3156 (1962).

34. N. E. Everds, "Hematology of the laboratory mouse," in *The Mouse in Biomedical Research* (Second Edition) (Elsevier, 2007), pp. 133–XVIII.

35. L. Wang, K. Maslov, J. Yao, B. Rao, and L. V. Wang, "Fast voice-coil scanning optical-resolution photoacoustic microscopy," Opt. Lett. **36**(2), 139–141 (2011).

36. K. D. Vandegriff and J. S. Olson, "The kinetics of O_2 release by human red blood cells in the presence of external sodium dithionite," J. Biol. Chem. **259**(20), 12609–12618 (1984).

37. K. Briely-Sabo and A. Bjornerud, "Accurate de-oxygenation of ex vivo whole blood using sodium Dithionite," in Proc. Intl. Sot. Mag. Reson. Med **8**, 2025 (2000).

38. J. Yao, L. Wang, J.-M. Yang, K. I. Maslov, T. T. W. Wong, L. Li, C.-H. Huang, J. Zou, and L. V. Wang, "High-speed label-free functional photoacoustic microscopy of mouse brain in action," Nat. Methods **12**(5), 407–410 (2015).

39. Z. Guo, S. Hu, and L. V. Wang, "Calibration-free absolute quantification of optical absorption coefficients using acoustic spectra in 3D photoacoustic microscopy of biological tissue," Opt. Lett. **35**(12), 2067–2069 (2010).

40. M. Nitzan and H. Taitelbaum, "The measurement of oxygen saturation in arterial and venous blood," IEEE Instrum. Meas. Mag. **11**(3), 9–15 (2008).